

Room-temperature storage of quantum entanglement using decoherence-free subspace in a solid-state spin system

F. Wang¹, Y.-Y. Huang¹, Z.-Y. Zhang^{1,2}, C. Zu¹, P.-Y. Hou¹, X.-X. Yuan¹, W.-B. Wang¹, W.-G. Zhang¹, L. He¹, X.-Y. Chang¹, L.-M. Duan^{1,2}

¹*Center for Quantum Information, IIIS, Tsinghua University, Beijing 100084, PR China*

²*Department of Physics, University of Michigan, Ann Arbor, Michigan 48109, USA*

(Dated: October 2, 2018)

We experimentally demonstrate room-temperature storage of quantum entanglement using two nuclear spins weakly coupled to the electronic spin carried by a single nitrogen-vacancy center in diamond. We realize universal quantum gate control over the three-qubit spin system and produce entangled states in the decoherence-free subspace of the two nuclear spins. By injecting arbitrary collective noise, we demonstrate that the decoherence-free entangled state has coherence time longer than that of other entangled states by an order of magnitude in our experiment.

PACS numbers:

INTRODUCTION

Decoherence caused by the system-environment interaction poses a serious obstacle to physical implementation of quantum information processing [1, 2]. Strategies involving active interventions, such as dynamical decoupling [3–10] and quantum error correction [11–14], have been extensively studied in experiments to recover quantum information from coupling with the environment [15–18]. Meanwhile, passive error control methods with no active recovery have also been proved to be efficient in preventing collective decoherence caused by symmetric system-environment coupling [19–26]. Quantum information in the decoherence-free subspace (DFS) does not decohere and is well protected even with perturbation in the system-environment interaction, making DFS an ideal quantum memory. DFS has been demonstrated in several experimental systems to protect single qubits from collective dephasing [27–30, 36].

In this paper, we present an experimental demonstration of DFS in a room-temperature solid-state system and use DFS to store quantum entanglement against general collective noise including both dephasing and dissipation. Quantum storage of single qubits has been demonstrated in a number of experimental systems, including trapped ions [37], single nuclear spins [36], atomic or spin ensembles [38–40]. To realize the full capability of quantum memory, it is important to further extend the information storage from single qubits to quantum entanglement. This extension is not straightforward as the best quantum memories demonstrated so far typically require good isolation of the qubits, which makes it difficult to generate entanglement between the qubits in the same system. Entanglement between nuclear spins coupled to the NV centers have been created in multiple works [17, 34, 36, 43–45]. Here we extend these works by demonstrating room-temperature storage of quantum entanglement in the DFS with two nuclear spins and the effectiveness of DFS under general collective noise. We produce entanglement between the nuclear spins within the DFS through universal gate control on the electronic and the nuclear spins. Under general collective noise, we demonstrate that the entangled state in DFS has coherence time longer than that of other entangled states by an order of magnitude.

RESULTS

Decoherence-free subspace

A DFS takes advantage of qubit-permutation symmetry in the system-environment interaction to isolate the stored quantum information from the environment. Therefore, evolution of quantum states inside a DFS is purely unitary. A simple example for a DFS is provided by the two-qubit subspace spanned by $|0\rangle_D = |0\rangle_{n1}|1\rangle_{n2}$ and $|1\rangle_D = |1\rangle_{n1}|0\rangle_{n2}$ when these two qubits are subject to collective dephasing noise [19, 20]. Apparently, a collective random phase ϕ accumulated for the basis states $|0\rangle \rightarrow e^{i\phi}|0\rangle$, $|1\rangle \rightarrow e^{-i\phi}|1\rangle$ cancel out in this subspace. Most of the experimental demonstrations focus on this special case [27, 28]. Under general collective noise including both dephasing and relaxation, the states $|0\rangle_D$ and $|1\rangle_D$ are not stable any more, but their combination, the singlet state $|S\rangle = (|0\rangle_{n1}|1\rangle_{n2} - |1\rangle_{n1}|0\rangle_{n2})/\sqrt{2}$ is still an entangled state lying within the DFS [22–24].

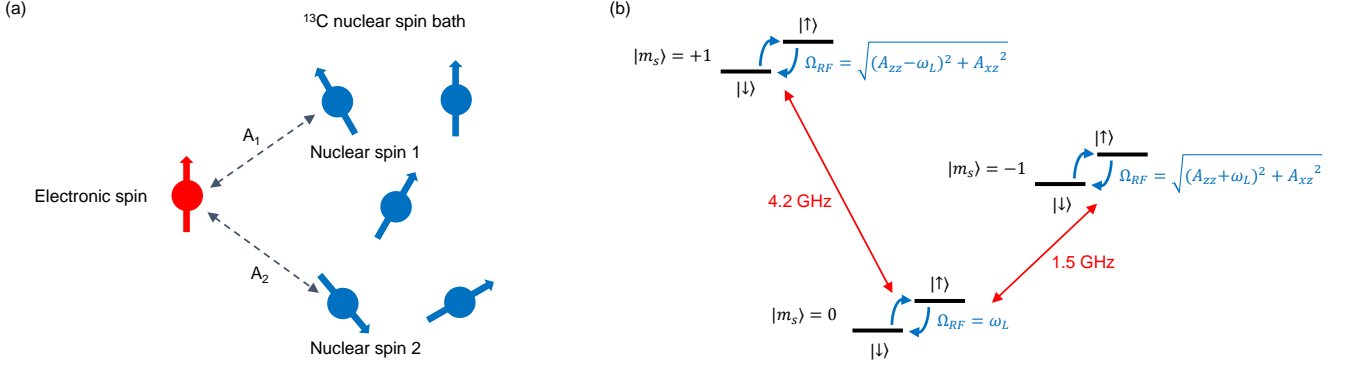


FIG. 1: Experimental system. (a) The NV electronic spin (red) and the coupled ^{13}C spin bath (Blue). Entanglement states are stored in two isolated weakly coupled ^{13}C nuclear spins. (b) Energy structure of the NV electronic spin and a weakly coupled nuclear spin. Nuclear spin sublevels $|\uparrow\rangle$ and $|\downarrow\rangle$ are split by Zeeman shift (ω_L) and hyperfine interaction (A_{zz} , A_{xz}) with $\omega_0 = \omega_L(m_s = 0)$, $\omega_{\pm 1} = \sqrt{(A_{zz} \mp \omega_L)^2 + A_{xz}^2}$ ($m_s = \pm 1$)

Control of two weakly coupled nuclear spins

We use two ^{13}C nuclear spins weakly coupled to an individual NV center electronic spin in a diamond crystal as our qubits (Fig. 1(a,b)). The NV electronic spin is a well characterized spin-1 system which can be optically initialized and readout [31], and coherently manipulated with microwave source at room temperature [32]. We use the NV electronic spin as a handle to coherently control and entangle the nuclear spins and read out their final state [33–35]. The external magnetic field provides a source of collective dephasing noise to the target nuclear spins. We prepare two typical entangled states $|T\rangle = (|0\rangle_{n1}|1\rangle_{n2} + |1\rangle_{n1}|0\rangle_{n2})/\sqrt{2}$ and $|S\rangle = (|0\rangle_{n1}|1\rangle_{n2} - |1\rangle_{n1}|0\rangle_{n2})/\sqrt{2}$ to demonstrate the DFS under the collective dephasing noise and find that the memory time is limited by the electronic spin relaxation time T_1 . To verify the DFS under arbitrary collective noise including both dephasing and relaxation, we realize a general collective noise model by injecting a noisy radio frequency field into the system [34, 41]. Under general collective noise, we show that the entangled state $|S\rangle$ within the DFS is still well protected until the electronic spin relaxation breaks the system-environment symmetry while the state $|T\rangle$ quickly decoheres.

The experiments are performed at room temperature on a diamond sample with an external magnetic field of 480 Gauss along the NV symmetry axis. We use the hyperfine interaction to coherently manipulate the nuclear spin by applying an equally-spaced sequence of π rotations (the Carr-Purcell-Meiboom-Gill, or CPMG sequence) to flip the electronic spin [17, 18, 35]. We use the XY8 sequence in our experiment to reduce the influence of imperfection in pulse durations and the accumulation of systematic pulse errors [16, 41]. The multi-pulse CPMG sequence decouples the electronic spin from the spin bath. At the same time, the electronic spin gets entangled with a specific nuclear spin when the pulse interval 2τ satisfies certain resonance condition, which leads to collapse of the electronic spin coherence after the CPMG sequence and thus can be detected. The resonance condition depends on A_{\parallel} , the parallel component of the hyperfine interaction for the specific nuclear spin, and is given by

$$2\tau \approx \frac{2(2k-1)\pi}{2\omega_L + A_{\parallel}}$$

where the integer k denotes the order of resonance and ω_L is the nuclear spin Larmor frequency. Based on this resonance, we control the total number of π pulses N and the pulse interval 2τ to complete single-bit operations (X or Z rotation) or conditional operation ($\pm X$ rotation conditional on the state of electronic spin) on the target nuclear spins, where X and Z denote the Pauli matrices σ_x and σ_z . For each type of gates, the condition for N depends on the transverse component of the hyperfine interaction A_{\perp} [47].

Calibration of hyperfine parameters

To perform high-fidelity gate operations on the weakly coupled nuclear spins, it is required to have precise calibration of the hyperfine interaction magnitudes A_{\parallel} and A_{\perp} for each target nuclear spins. The hyperfine parameters can be

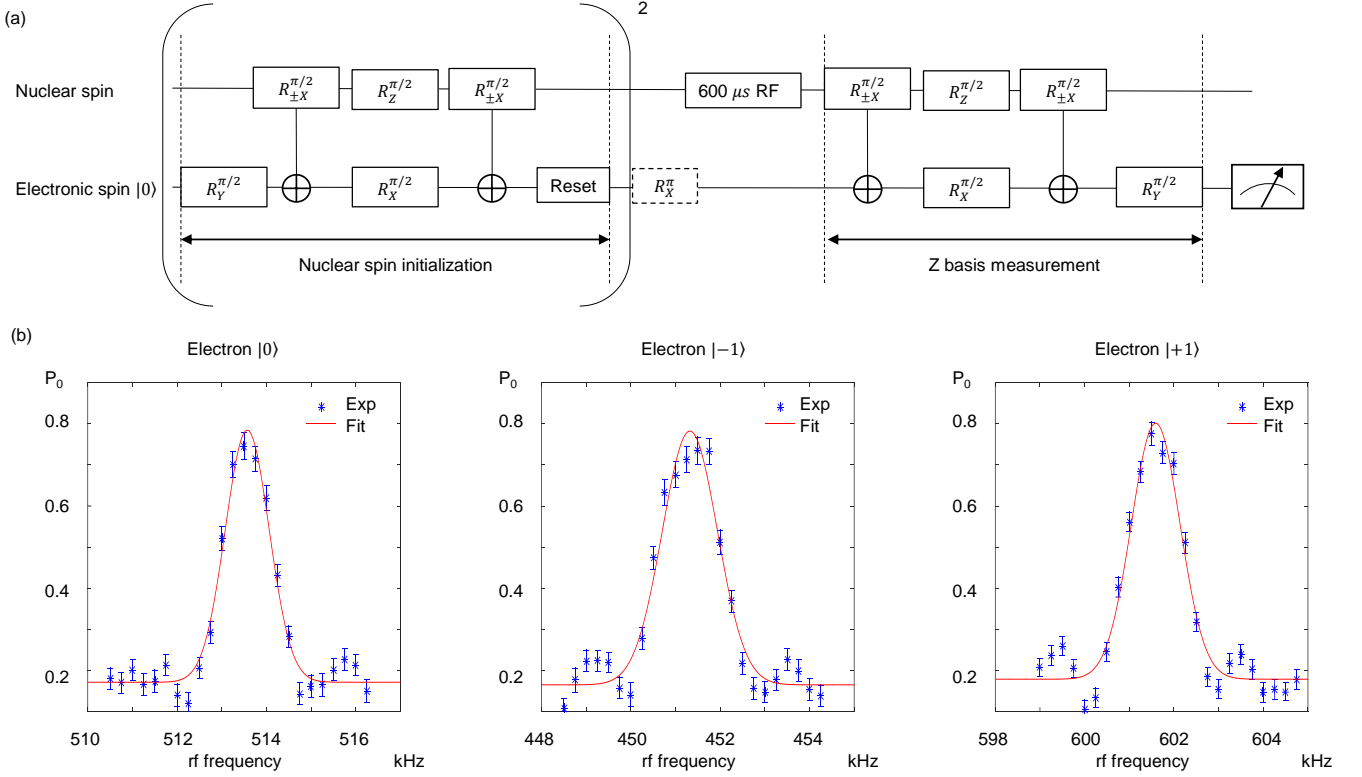


FIG. 2: Calibration of the nuclear spin hyperfine interaction parameters. (a) Gate sequence to scan the resonant frequency of nuclear spins with the electronic spin set at $m_s = +1, 0, -1$ states, respectively. The nuclear spin is initialized by swapping the electronic spin polarization onto the nuclear spin. Electronic spin is reset to $|0\rangle$ or $|\pm 1\rangle$ state using a 350 ns green laser or an additional π rotation afterwards. A rf pulse with a duration of 600 μs and a scanning frequency is then implemented on the nuclear spin to trigger spin flips at resonant frequency. The final state readout is accomplished by swapping the nuclear spin state back onto the electronic spin. (b) Probability of electronic spin in $m_s = 0$ state (P_0) as a function of the rf frequency with the electronic spin at $m_s = 0, -1, +1$ states, respectively, for nuclear spin 1. Solid lines are the Gaussian fits. See the supplementary material for results on the nuclear spin 2.

calibrated with a resolution about 10 kHz by fitting the experimental data on the measured electronic spin coherence after the CPMG sequence to the numerical simulation of the corresponding dynamics with the fitting parameters A_{\parallel} and A_{\perp} . However, as the gate fidelity is strongly correlated with the precision of the hyperfine parameters, the 10 kHz resolution in calibration is not enough for achieving high-fidelity quantum gates on the nuclear spins. We describe a method based on the nuclear spin ODMR (Optical Detected Magnetic Resonance) for high-precision calibration of A_{\parallel} and A_{\perp} in experiments. We measure the resonant frequency of the nuclear spins with the electronic spin set at $m_s = +1, 0, -1$ respectively. As described in Fig. 2(a), with rough calibration of the hyperfine parameters by the CPMG sequence, we first polarize the nuclear spin (with significant imperfection) by swapping the electronic spin polarization onto the nuclear spin, and optically reset the electronic spin to $m_s = 0$ state (or $m_s = \pm 1$ state by another resonant microwave π rotation). After that, we apply a π -pulse of 600 μs duration on the target nuclear spin using radio frequency field and measure the nuclear spin flip probability by swapping the nuclear spin polarization back onto the electronic spin. In Fig. 2(b), we show that this approach gives a resonant frequency with a standard deviation of 0.05 kHz, thus allows us to determine the nuclear spin hyperfine parameter to a resolution about 0.05 kHz in the parallel component A_{\parallel} and about 0.5 kHz in the transverse component A_{\perp} [47].

After the hyperfine parameters are precisely calibrated, we perform the desired gate (conditional X gate, unconditional X and Z gate) on the polarized nuclear spins with electronic spin at $m_s = 0$ or $m_s = -1$ state. To estimate the gate fidelity, we apply the same gate 10 times, and from the slow decay of the target state fidelity as shown in Fig. 3 and the supplementary material, we extract a gate fidelity about $F \approx 0.988$ ($F \approx 0.975$) for the conditional operations on nuclear spin 1 (spin 2). Gate fidelity for nuclear spin 1 is slightly higher than that for nuclear spin 2, because nuclear spin 1 has a larger parallel component of hyperfine parameters, which leads to a shorter gate time

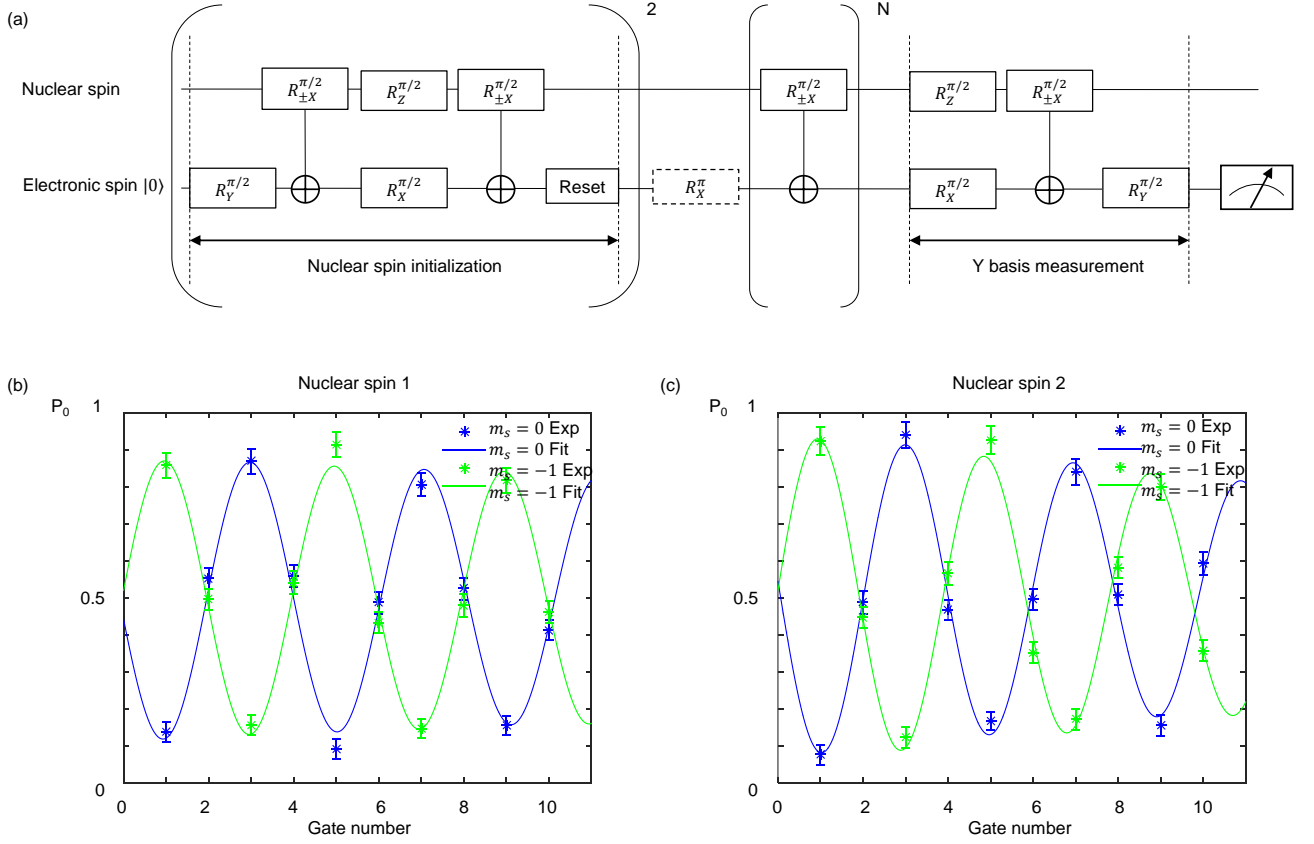


FIG. 3: Characterization of the conditional X gate on nuclear spins 1 and 2. See the supplementary material for results on unconditional gates. (a) Experimental scheme to characterize the gate fidelity. The nuclear spin is polarized by swapping the electronic spin polarization onto the nuclear spin. An additional π rotation is applied to set the electronic spin to $m_s = -1$ state. After that, the desired gate (conditional X gate) is applied on the nuclear spin for N times ($N = 1, \dots, 10$) with the electronic spin at $m_s = 0$ or $m_s = -1$ before measuring the nuclear spin on the Y basis. (b,c) Experimental results of conditional X gate on the nuclear spin 1 and 2, respectively. The nuclear spin rotates on the opposite direction of the X axis with the electronic spin at $m_s = 0, -1$ states. Solid lines are fits by the function $\sin(2\pi N/4)(1 - bN)$ with $b = 0.012$ and a standard deviation of $\sigma = 0.011$ in (b) and $b = 0.025$ and a standard deviation of $\sigma = 0.014$ in (c). The results are without correction of initialization and detection error.

[47]. Using the high fidelity conditional X gate and the unconditional Z gate, single nuclear spin initialization and readout fidelity is enhanced to $F_1 = 0.896(6)$ and $F_2 = 0.873(9)$ for nuclear spin 1 and 2 [47].

Entanglement preparation

We prepare two typical entangled states $|T\rangle$ and $|S\rangle$ for the nuclear spins using the above gates. When the nuclear spins are subject to collective dephasing noise, both the two states are decoherence free. However, only the entangled state $|S\rangle$ is protected under arbitrary collective noise. To produce the desired entangled states, as shown in Fig. 4(a), we first prepare an electron-nuclear entangled state $(|0\rangle_e|Y_-\rangle_{n2} - i|1\rangle_e|Y_+\rangle_{n2})/\sqrt{2}$ by applying a conditional $\pi/2$ operation on the polarized nuclear spin 2 with the electronic spin set at $(|0\rangle - i|1\rangle)/\sqrt{2}$ state, where $|Y_{\pm}\rangle$ denotes the eigenstate of σ_y with ± 1 eigenvalue. After that, we coherently swap the states between the electronic spin and the nuclear spin 1 by applying a sequence of gate operations as shown in Fig. 4(a), and subsequently implement a single-bit X gate on the nuclear spin 1 to produce the target entangled states within the DFS of the two nuclear spins. By controlling the phase ϕ of the swap gate we are able to prepare the entangled state to either $|T\rangle$ or $|S\rangle$. The entangled state fidelity is characterized by calculating the overlap between the experiment density matrix ρ_{exp} constructed through quantum state tomography [47] and the target ideal state $|\Psi_{id}\rangle$ through $F = \langle \Psi_{id} | \rho_{exp} | \Psi_{id} \rangle$. With the measured fidelity $F = 0.60(1)$ for $|S\rangle$ state and $F = 0.59(1)$ for $|T\rangle$ state (without correction of initialization

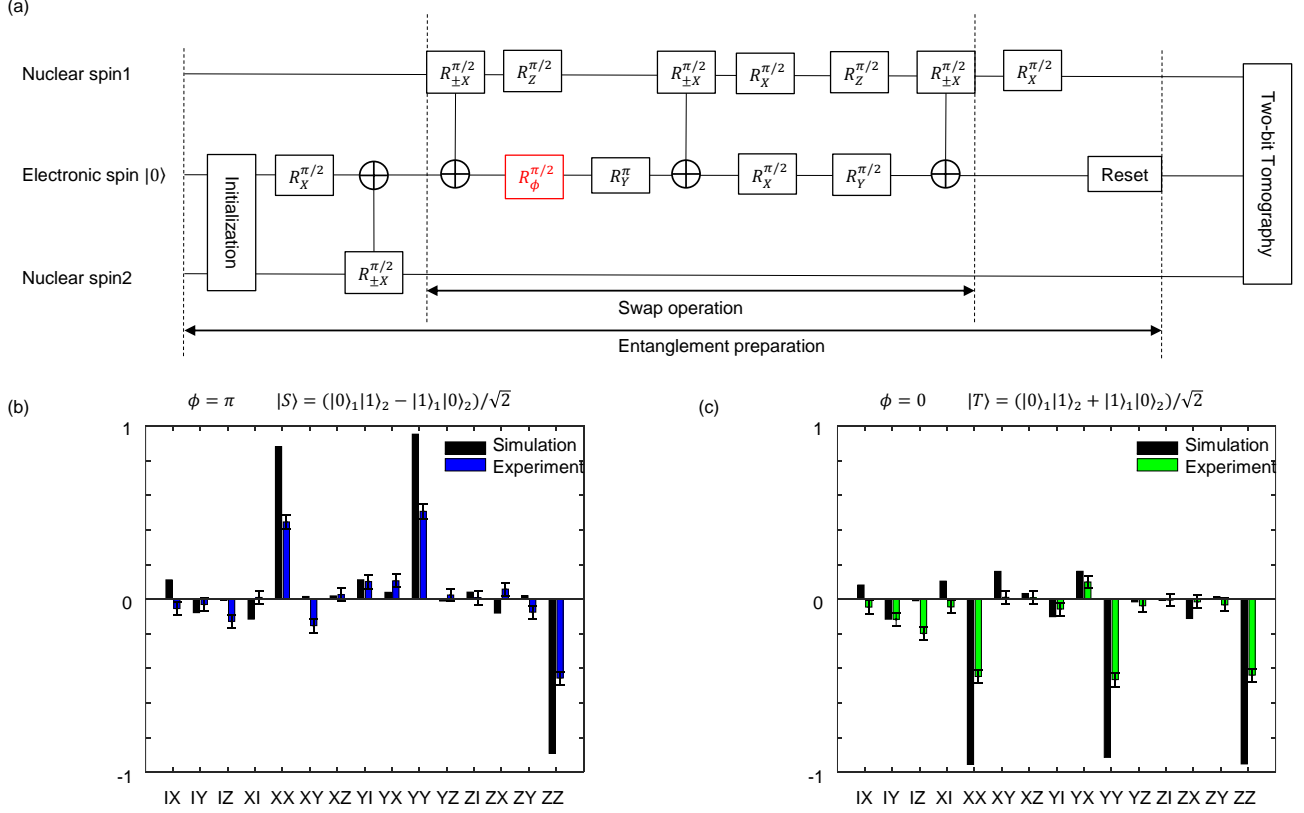


FIG. 4: Preparation and detection of entangled states between the nuclear spins. (a) Gate sequence to prepare entangled states between nuclear spins at room temperature. Entanglement is first generated between the nuclear spin 2 and the electronic spin. By swapping the electronic spin with the nuclear spin 1, entanglement between nuclear spins is produced. A subsequent $\pi/2$ rotation is applied to prepare the entangled state in the DFS. The phase ϕ of the operation in red is controlled to produce $|T\rangle$ state ($\phi = 0$) or $|S\rangle$ state ($\phi = \pi$). The readout is performed by quantum state tomography on the two nuclear spins [47]. (b,c) Quantum state tomography results for $|S\rangle$ state (b) and $|T\rangle$ state (c). Black bar describes the simulation result [47], blue (green) bar is the experiment data for $|S\rangle$ ($|T\rangle$) state without correction of initialization and readout errors.

and detection error), we demonstrate entanglement between the nuclear spins (Fig. 4(b,c)).

Various imperfections affect the entangling process, which leads to a low entangled state fidelity. We summarize the four major contributions. (i) The preparation process involves the initialization of nuclear spin 2, with a single-qubit initialization and readout fidelity about 0.87, we expect a similar fidelity drop in term of the entanglement fidelity. (ii) The use of green laser at the end of the entangling process to optically reset the electronic spin decreases the nuclear spin fidelity in both polarization and coherence [17, 42]. (iii) The intrinsic errors mostly caused by the crosstalk between the targeted two nuclear spins decrease the entangled state fidelity from 1 to 0.95 in our numerical simulation (see Fig. 4(b,c)). (iv) Decoherence, magnetic field fluctuation and gate error accumulation in each experimental run (note that the whole state preparation process requires application of more than ten gates) reduce the final state fidelity over the 10^6 repetitions of experiments for measurement of each density matrix element [47]. At room temperature, due to these limitations, it is hard to significantly improve the entanglement fidelity for the nuclear spins. With an isotopically purified samples, the coherence time for the electronic spin increases, but it becomes more difficult to find nuclear spins with appropriate hyperfine interaction strength for the entangling gates. If we put the sample in a cryogenic environment, both the initialization fidelity and the coherence time for the electronic spin would be significantly improved, and correspondingly the entanglement fidelity for the nuclear spins will increase substantially [36].

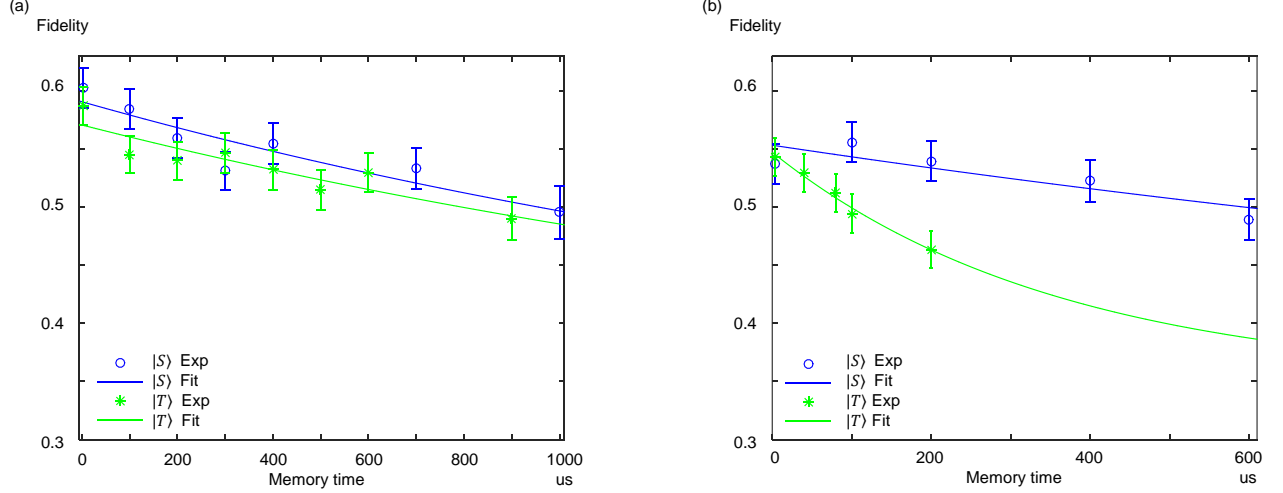


FIG. 5: Decay of the entanglement fidelity under various noise environments. (a) Entanglement fidelity as a function the storage time t under collective dephasing noise. Solid lines are fits to $\exp(-t/T_{est})$ with $T_{est} = 2.24$ ms and a standard deviation of $\sigma = 153$ μs for $|S\rangle$ state (blue) and $T_{est} = 2.29$ ms and a standard deviation of $\sigma = 232$ μs for $|T\rangle$ state (green). The fitting curves saturate at 0.35, which corresponds to the fidelity of the final state when all the coherence terms drop to zero. Due to the limited fidelity for initial state preparation, the population is not given by an identity matrix, so the saturation fidelity is 0.35 instead of 0.5. (b) Entanglement fidelity as a function of the storage time t under general collective noise. Solid lines are fits to $\exp(-t/T_{est})$ with $T_{est} = 2.18$ ms and a standard deviation of $\sigma = 366$ μs for $|S\rangle$ state (blue) and $T_{est} = 360$ μs and a standard deviation of $\sigma = 20$ μs for $|T\rangle$ state (green).

Test of DFS under collective dephasing noise

We start by exploring DFS with the system subject to a collective dephasing noise, which in our case is the external magnetic field. In Fig 5(a), we prepare the nuclear spins in the DFS and measure their state fidelity extracted from quantum state tomography as a function of storage time. By fitting the data to $\exp(-t/T_{est})$, we extracted a memory time of $T_{est} \approx 2.3$ ms, which is limited by the electronic spin relaxation time $T_1 \approx 2.5$ ms. This can be explained by the breakup of the system-environment coupling symmetry. As the electronic spin relaxes, it causes independent dephasing noise for the two nuclear spins with $\Delta\omega \approx |A_{||1} - A_{||2}| \approx 148$ kHz, which destroys the state quickly [36]. Longer memory time could be achieved for entangled states if one makes use of the isotopically purified diamond samples to reduce the nuclear spin crosstalk error with spin bath and repeatedly polarizes the electronic spin to mitigate the dephasing noise [42]. Alternatively, if one put the diamond sample in the cryogenic environment, both the entanglement fidelity and entanglement storage time can be significantly improved as the electronic spin relaxation time gets much longer under low temperature [46].

Test of DFS under general collective noise

A crucial step to verify DFS is to investigate the state coherence under general collective noise including both dephasing and relaxation. To realize general collective noise in addition to the dephasing induced by the external magnetic field, we introduce collective relaxation by injecting a noisy radio-frequency field. Because the magnetic field couples the nuclear spins identically, the relaxation induced by the injected rf field is collective to nuclear spins in the close neighborhood of the electronic spin. In Fig. 5(b), We compare the storage time of two typical entangled states $|T\rangle$ and $|S\rangle$. In agreement with theory, only $|S\rangle$ state which lies within the DFS under arbitrary collective noise is protected against the injected noise with a fitted memory time $T_{est} \approx 2.2$ ms. In comparison, $|T\rangle$ state is destroyed quickly with a fitted memory time $T_{est} \approx 360$ μs .

SUMMARY

In summary, we have demonstrated room temperature storage of quantum entanglement by preparing quantum states in the DFS of two nuclear spins and experimentally verified that the entangled state within the DFS has coherence time significantly longer than that of other components under general collective noise. Storage of quantum entanglement is required in many quantum information protocols and our result suggests that the DFS could find interesting applications in experimental realization of those protocols.

We thank T. H. Taminiau for discussions. This work was supported by Tsinghua University and the Ministry of Education of China. LMD and ZYZ acknowledge in addition support from the AFOSR MURI and the ARL CDQI program.

-
- [1] W. G. Unruh, Phys. Rev. A 51, 992 (1995).
 - [2] D. P. DiVincenzo, Fortschritte der Physik 48, p. 771 (2000).
 - [3] L. Viola and S. Lloyd, Phys. Rev. A 58, 2733 (1998).
 - [4] P. Zanardi, Phys. Lett. A 258, 77 (1999).
 - [5] L.-M. Duan and G. Guo, Phys. Lett. A 261, 139 (1999).
 - [6] D. Vitali and P. Tombesi, Phys. Rev. A 59, 4178 (1999).
 - [7] L. Viola, E. Knill, and S. Lloyd, Phys. Rev. Lett. 82, 2417 (1999).
 - [8] L. Viola and E. Knill, Phys. Rev. Lett. 90, 037901 (2003).
 - [9] K. Khodjasteh and D. A. Lidar, Phys. Rev. Lett. 95, 180501 (2005).
 - [10] H. K. Ng, D. A. Lidar, J. Preskill, Phys. Rev. A 84, 012305 (2011).
 - [11] P. W. Shor, Phys. Rev. A 52, R2493 (1995).
 - [12] A. M. Steane, Phys. Rev. Lett. 77, 793 (1996).
 - [13] A. R. Calderbank and P. W. Shor, Phys. Rev. A 54, 1098 (1996).
 - [14] A. M. Steane, Proc. R. Soc. London A 452, 2551 (1996).
 - [15] G. de Lange, Z. H. Wang, D. Riste, V. V. Dobrovitski, R. Hanson, Science 330, 60 (2010).
 - [16] C. A. Ryan, J. S. Hodges, and D. G. Cory, Phys. Rev. Lett. 105, 200402 (2010).
 - [17] T. H. Taminiau, J. Cramer, T. van der Sar, V. V. Dobrovitski and R. Hanson, Nature Nanotech. 9, 171-176 (2014).
 - [18] J. Cramer, N. Kalb, M. A. Rol, B. Hensen, M. S. Blok, M. Markham, D. J. Twitchen, R. Hanson and T. H. Taminiau, Nat. Commun. 7: 11526 (2016).
 - [19] G. M. Palma, K.-A. Suominen and A. K. Ekert, Proc. Roy. Soc. London Ser. A 452: 567 (1996).
 - [20] L.-M. Duan and G.-C. Guo, Phys. Rev. Lett. 79, 1953 (1997);
 - [21] L.-M. Duan and G.-C. Guo, Phys. Rev. A, 57, 737 (1998).
 - [22] P. Zanardi and M. Rasetti, Phys. Rev. Lett. 79, 3306 (1997).
 - [23] P. Zanardi and M. Rasetti, Mod. Phys. Lett. B, 11, 1085 (1997).
 - [24] D. A. Lidar, D. Bacon and K. B. Whaley, Phys. Rev. Lett. 81, 2594 (1998).
 - [25] D. A. Lidar, D. Bacon, J. Kempe and K. B. Whaley, Phys. Rev. A, 63, 022306 (2001).
 - [26] D. A. Lidar and K. B. Whaley, Springer Lecture Notes in Physics 622 (2003)
 - [27] P. G. Kwiat, A. J. Berglund, J. B. Altepeter and A. G. White, Science, 290, 498 (2000).
 - [28] D. Kielpinski, V. Meyer, M. A. Rowe, C. A. Sackett, W. M. Itano, C. Monroe and D. J. Wineland, Science, 291, 1013 (2001).
 - [29] E. M. Fortunato, L. Viola, J. Hodges, G. Teklemariam and D. G. Cory, New J. Phys 4:5 (2002).
 - [30] L. Viola, E. M. Fortunato, M. A. Pravia, E. Knill, R. Laflamme, D. G. Cory, Science, 293, 2059 (2001).
 - [31] J. Wrachtrup and F. Jelezko, J. Phys: Condens. Matter, 16, R1089 (2004).
 - [32] F. Jelezko, T. Gaebel, I. Popa, A. Gruber and J. Wrachtrup, Phys. Rev. Lett. 92, 076401 (2004).
 - [33] M. V. Gurudev Dutt, L. Childress, L. Jiang, E. Togan, J. Maze, F. Jelezko, A. S. Zibrov, P. R. Hemmer, M. D. Lukin, Science 316, 1312 (2007).
 - [34] T. van der Sar, Z. H. Wang, M.S. Blok, H. Bernien, T. H. Taminiau, D. M. Toyli, D. A. Lidar, D. D. Awschalom, R. Hanson and V. V. Dobrovitski, Nature, 484, 82-86 (2012).
 - [35] T. H. Taminiau, J. J. T. Wagenaar, T. van der Sar, F. Jelezko, V. V. Dobrovitski and R. Hanson, Phys. Rev. Lett. 109, 137602 (2012).
 - [36] A. Reiserer, N. Kalb, M. S. Blok, K. J. M. van Bemmelen, T. H. Taminiau and R. Hanson, Phys. Rev. X 6, 021040 (2016).
 - [37] Y. Wang, M. Um, J.-H. Zhang, S.-M. An, M. Lyu, J.-N. Zhang, L.-M. Duan, D. Yum, K. Kim, arxiv/1701.04195 and refs therein.
 - [38] A. I. Lvovsky, W. Tittel, and B. Sanders, Nature Photon. 3, 706-714 (2009);
 - [39] M. Zhong, M. P. Hedges, R. L. Ahlefeldt, J. G. Bartholomew, S. E. Beavan, S. M. Wittig, J. J. Longdell, and M. J. Sellars, Nature 517, 177-180 (2015).
 - [40] Y. O. Dudin, L. Li, A. Kuzmich, Phys. Rev. A 87, 031801(R) (2013).
 - [41] F. Wang, C. Zu, L. He, W.-B. Wang, W.-G. Zhang, L.-M. Duan, Phys. Rev. B 94, 064304 (2016).

- [42] L. Jiang, J. S. Hodges, J. R. Maze, P. Maurer, J. M. Taylor, D. G. Cory, P. R. Hemmer, R. L. Walsworth, A. Yacoby, A. S. Zibrov, M. D. Lukin, *Science*, 326, 267 (2009).
- [43] P. Neumann, N. Mizuochi, F. Rempp, P. Hemmer, H. Watanabe, S. Yamasaki, V. Jacques, T. Gaebel, F. Jelezko, J. Wrachtrup, *Science*, 320, 1326 (2008).
- [44] G. Waldherr, Y. Wang, S. Zaiser, M. Jamali, T. Schulte-Herbruggen, H. Abe, T. Ohshima, J. Isoya, J. F. Du, P. Neumann, J. Wrachtrup, *Nature* 506, 204(2014).
- [45] Wolfgang Pfaff, Tim H. Taminiau, Lucio Robledo, Hannes Bernien, Matthew Markham, Daniel J. Twitchen, Ronald Hanson, *Nature Phys.* 9, 29 (2013).
- [46] J. Cramer, N. Kalb, M. A. Rol, B. Hensen, M. S. Blok, M. Markham, D. J. Twitchen, R. Hanson, T. H. Taminiau, *Nat. Commun.* 7: 11526 (2016).
- [47] Supplementary materials.

Supplementary Material "Room temperature entanglement storage using decoherence free subspace in a solid-state spin system"

F. Wang¹, Y.-Y. Huang¹, Z.-Y. Zhang^{1,2}, C. Zu¹, P.-Y. Hou¹, X.-X. Yuan¹, W.-B. Wang¹, W.-G. Zhang¹, L. He¹, X.-Y. Chang¹, L.-M. Duan^{1,2}

¹*Center for Quantum Information, IIIS, Tsinghua University, Beijing 100084, PR China*

²*Department of Physics, University of Michigan, Ann Arbor, Michigan 48109, USA*

(Dated: October 2, 2018)

In this supplementary material, we include experimental details and numerical simulation for parameter calibration, quantum gates, and state detection in weakly coupled nuclear spin systems. We also describe experimental technique to control environment and realize general collective noise model.

PACS numbers:

EXPERIMENTAL SETUP

The optical setup is similar to what was described in Ref [1]. A major difference is that another acoustic optical modulator (AOM) in double pass configuration is added into the optical path right after the first AOM double pass to constrain the leakage of green laser to a higher order.

The microwave signal is delivered into the system with a waveguide transmission line fabricated on a cover glass, to which the diamond sample is attached. The microwave field is generated by a carrier signal modulated at an IQ mixer by two analog outputs of an Arbitrary Waveform Generator (AWG) to control the relative phase of the signal. We add a switch controlled by the digital output of the AWG after the IQ mixer to reduce the influence of leakage of the carrier signal. The microwaves are then sent to a high power amplifier and subsequently get delivered to the sample.

The radio frequency signal is generated by the analog channel of the AWG and amplified through a high power amplifier. We fabricated a coplanar coil with matching impedance on a PCB board to deliver radio frequency signal. To achieve a reasonable nuclear spin Rabi frequency, the coil is detached from the diamond surface with a distance about 2 mm (The other surface is attached to the cover glass).

A magnetic field of $B_z = 480$ Gauss is applied along the NV symmetry axis using a permanent magnet. The strong magnetic field is used to polarize the intrinsic nitrogen spin and provide a relative strong Larmor frequency to the nuclear spins compared to the nuclear spin hyperfine parameters. All the experiments are performed at room temperature with 10^6 repetitions for measurement of each data point.

CALIBRATION OF NUCLEAR-SPIN HYPERFINE INTERACTION PARAMETERS

Due to the anisotropic property of the hyperfine interaction, nuclear spins undergo different evolutions with electronic spin at different eigenstates $m_s = +1, 0, -1$. We consider the two-spin system composed of an electronic spin with $m_s = 0$ and $m_s = -1$, denoted as $|0\rangle$ and $|1\rangle$, and a nuclear spin with components of the spin operator denoted as I_x, I_y, I_z . With the electronic spin at $|0\rangle$ and $|1\rangle$ state, the nuclear spin Hamiltonian is denoted as H_0 and H_1 , respectively, which takes the form

$$H_0 = \omega_L I_z, \quad (1)$$

$$H_1 = (\omega_L + A_{\parallel})I_z + A_{\perp}I_x, \quad (2)$$

where ω_L is the nuclear Larmor frequency, A_{\parallel} and A_{\perp} are the parallel and transverse components of the hyperfine parameters. Consider a simple equally-spaced sequence of π rotations $(\tau - \pi - 2\tau - \pi - \tau)$ with pulse number $N = 2$ and pulse interval denoted by 2τ , the net result of this specific decoupling sequences is that the nuclear spin rotates by an angle of ϕ around axis \hat{n}_0 (\hat{n}_1) with the electronic spin at $m_s = 0$ ($m_s = -1$) state. When $\hat{n}_0 \cdot \hat{n}_1 = -1$, a resonance condition is satisfied and the electronic spin gets entangled with the nuclear spin, thus the electronic coherence collapses after the CPMG sequence (Fig. 1 grey). With $\omega_L \gg A_{\parallel}, A_{\perp}$, the condition of resonance is given

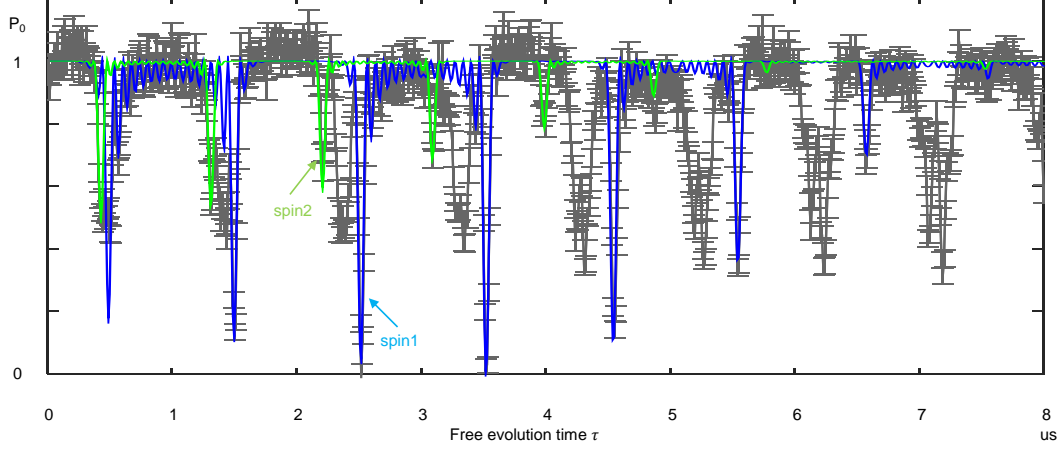


FIG. 1: Calibration of nuclear spin environment by the CPMG pulse sequence. What is shown is the measured coherence signal after the CPMG decoupling sequence as a function of free evolution time τ . The signal (grey) is taken with a magnetic field $B = 490$ Gauss by preparing the electronic spin in $(|0\rangle - i|1\rangle)/\sqrt{2}$ state and applying a XY8 sequence with 16 π rotations before measuring the electronic spin coherence by another $\pi/2$ rotation around the $-X$ axis. The free precession time τ is taken with a step of 10 ns . Blue(green) is simulation with hyperfine parameters calibrated from the nuclear spin ODMR signal for spin 1 (spin 2).

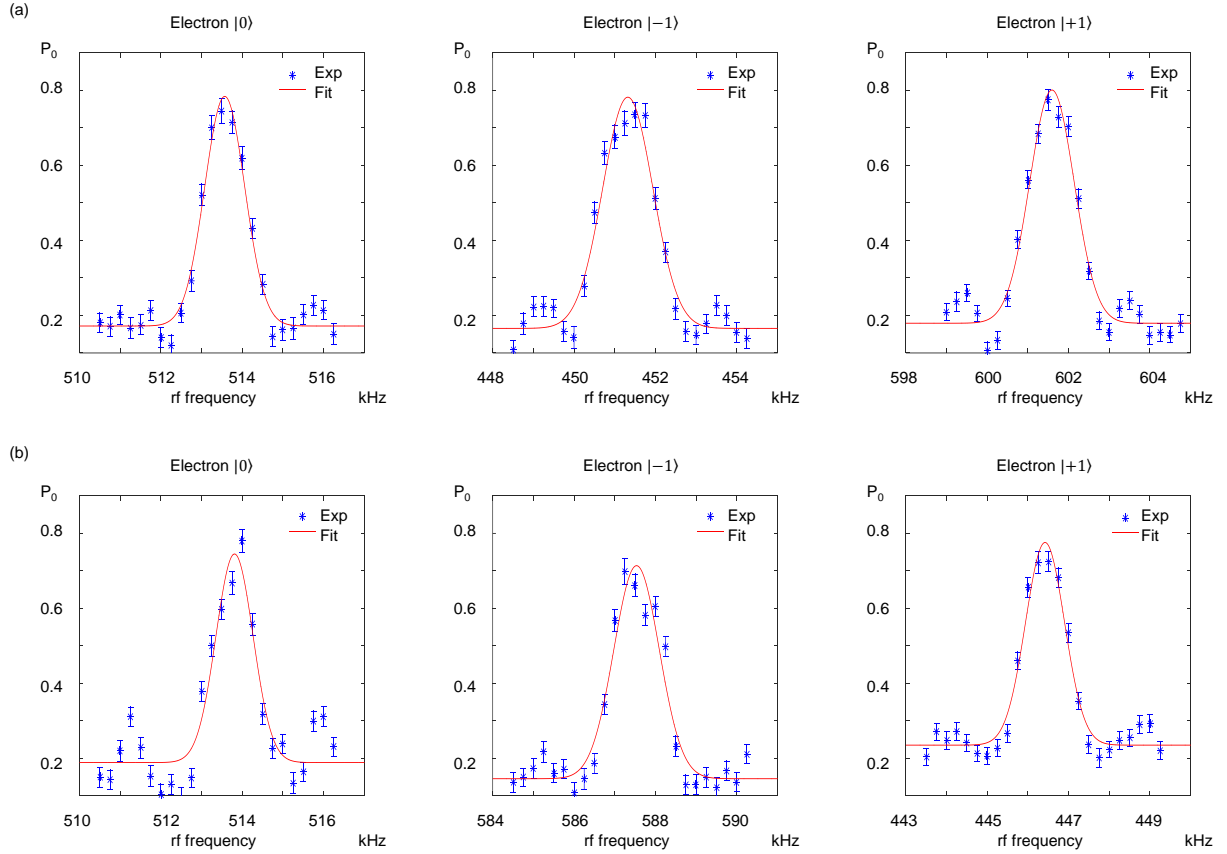


FIG. 2: Nuclear spin ODMR results for spin 1 and spin 2. The experimental scheme is illustrated in Fig. 1 in the main text. (a,b) Resonant frequency with electronic spin at $m_s = +1, 0, -1$ state for nuclear spin 1 and 2.

TABLE I: Spin1, Spin2: gate parameters in the experiment

	U	$\tau(\mu s)$	N	total time(μs)
spin1	$R_X^e(\pi/2)$	2.579	7	36.1
	$R_X(\pi/2)$	4.123	8	66.0
	$R_Z(\pi/2)$	0.047	4	0.4
spin2	$R_X^e(\pi/2)$	2.253	19	85.6
	$R_Z(\pi/2)$	0.039	4	0.3

by [2]

$$\tau \approx \frac{(2k-1)\pi}{2\omega_L + A_{\parallel}} \quad (3)$$

where k is the order of resonance. The probability that the coherence is preserved is given by [2]

$$P = (M+1)/2, \quad (4)$$

$$M = 1 - (1 - \hat{n}_0 \cdot \hat{n}_1) \sin^2 \frac{N\phi}{2} \quad (5)$$

At resonance, with $\omega_L \gg A_{\parallel}, A_{\perp}$, this equation becomes [2]

$$P = (\cos(Nm_x) + 1)/2, \quad (6)$$

$$m_x = \frac{A_{\perp}}{\sqrt{(A_{\parallel} + \omega_L)^2 + A_{\perp}^2}} \quad (7)$$

By fitting the experimental data on the measured electronic spin coherence after the CPMG sequence to the numerical simulation of the corresponding dynamics with the fitting parameters A_{\parallel} and A_{\perp} , single nuclear spins can be resolved to a resolution of about 10 kHz [2]. As illustrated in the main text, to calibrate the nuclear spin hyperfine parameters more precisely, we run nuclear spin ODMR experiments with the electronic spin set at $m_s = +1, 0, -1$ states (Fig. 2). With the nuclear spin ODMR technique, the hyperfine parameters for the two nuclear spins used in our experiment are determined with a high precision as follows:

$$A_{\parallel 1} = -77.02(3) \text{ kHz}, \quad A_{\perp 1} = 114.5(1) \text{ kHz}, \quad (8)$$

$$A_{\parallel 2} = 71.03(3) \text{ kHz}, \quad A_{\perp 2} = 58.7(3) \text{ kHz}, \quad (9)$$

where the number in the bracket denotes the standard deviation on the last digit.

CONTROL OF THE TWO WEAKLY COUPLED NUCLEAR SPINS

The conditional and unconditional gates are accomplished by the same pulse sequence used to calibrate the nuclear spin hyperfine interaction parameters. The parameters τ and N (Table I) in each gate are calculated using the calibrated hyperfine parameters. In Fig. 3, Fig. 4, and Fig. 5, we apply the same gates (conditional X gate, unconditional X gate, or unconditional Z gate) N times (with $N = 1, \dots, 10$) on the polarized nuclear spin with the electronic spin initialized at different states.

The gate fidelity is mainly restricted by three factors: (i) The precision of the hyperfine interaction parameters. (ii) The fluctuation of magnetic field. (iii) The decoherence of the electronic spin during the pulse sequence. To suppress the influence from the latter one, we choose two nuclear spins with hyperfine parameters A_{\parallel} around $\pm 50 \text{ kHz}$ so that they can be isolated from each other and the spin bath even at a small pulse interval τ . Therefore, the gate time can be controlled within 100 μs and decoherence contribution by the electronic spin to the gate infidelity is mitigated. From the slow decay of the oscillations in Fig. 3, Fig. 4 and Fig. 5, we estimate a gate fidelity of $F \sim 0.988$ (0.975) for the conditional X-gate on the nuclear spin 1 (2). The conditional gate on the nuclear spin 2 has a lower fidelity as its pulse sequence has a longer time and thus a larger contribution from the electronic spin decoherence. The unconditional gate has a higher intrinsic fidelity: we do not see noticeable fidelity decay after 10 gates under experimental uncertainty, suggesting its intrinsic fidelity $F > 99\%$.

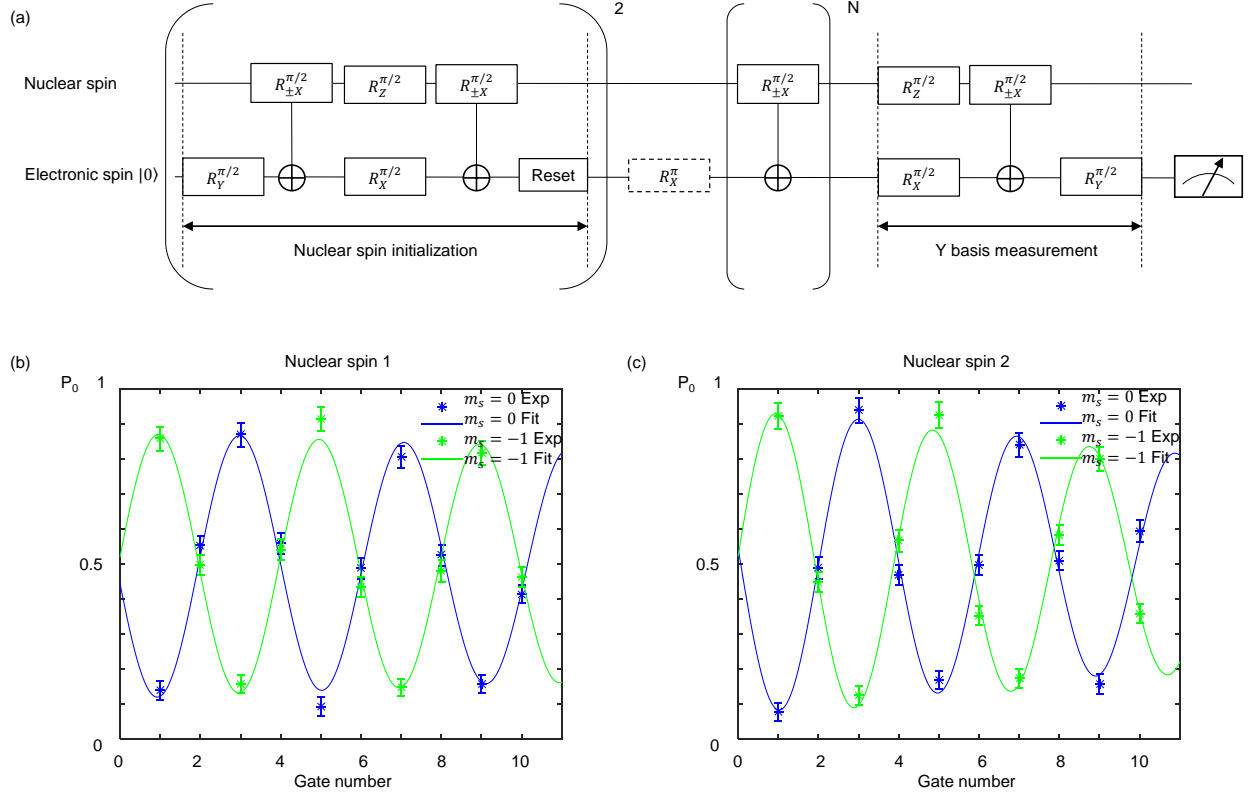


FIG. 3: Characterization of the conditional X gate for nuclear spin 1 and 2. (a) Experimental scheme. The nuclear spin is polarized by swapping the electronic spin polarization onto the nuclear spin. An optional π rotation is applied to set the electronic spin to $m_s = -1$ state. After that, the desired gate is applied on the nuclear spin for $N = 1, \dots, 10$ times with electronic spin at $m_s = 0$ or $m_s = -1$ separately before measuring the nuclear spin on the Y basis. (b,c) Characterization of conditional X gate for nuclear spin 1 and 2. Solid lines are fit by the formula $\sin(2\pi N/4) * (1 - bN)$ with $b = 0.012$ and a standard deviation $\sigma = 0.011$ in (b), and with $b = 0.025$ and a standard deviation $\sigma = 0.014$ in (c).

INITIALIZATION AND READOUT OF SINGLE NUCLEAR SPINS

The single nuclear spin initialization and readout is obtained by measuring the free evolution contrast of the nuclear spin coherence. In Fig. 6, the nuclear spin is prepared to $(|0\rangle - i|1\rangle)/\sqrt{2}$ with the electronic spin at $m_s = 0$ ($m_s = -1$) for nuclear spin 1 (spin 2). We characterize the nuclear spin coherence by projecting the nuclear spin phase to the electronic spin population. We repeat the initialization process twice and extract an initialization and readout fidelity of $F_1 = 0.896(6)$ and $F_2 = 0.873(9)$ for nuclear spin 1 and 2.

In experiments the initialization and readout fidelity of nuclear spins are always combined together as there is no direct ways to polarize or measure the state of nuclear spins separately. From the supplementary information of Ref. [6], the high initialization and readout fidelity indicates that the charge state initialization fidelity is either high (> 0.8 from our experiment result) or not sensitive to the measurements. We briefly summarize the arguments here respectively under the following two assumptions (i) the re-initialization has no memory for the charge state or (ii) the re-initialization does not change the charge state.

Consider green laser initialization involves both spin states and charge states, the initial state of the electronic spin takes the form:

$$\rho_e = p_1\rho_0 + p_2\rho_m + p_3\rho_s + p_4\rho_c \quad (10)$$

where ρ_0 is the desired $m_s = 0$ state, ρ_m denotes the completely mixed state of $m_s = 0$ and $m_s = -1$ states, ρ_s denotes the other spin state $m_s = +1$, and ρ_c denotes the NV^0 state. The probabilities satisfy the normalization $p_1 + p_2 + p_3 + p_4 = 1$. In our normalized fluorescence contrast measurement, the $m_s = 0$ state gives a signal of 1, $m_s = \pm 1$ states and NV^0 give a signal of 0.

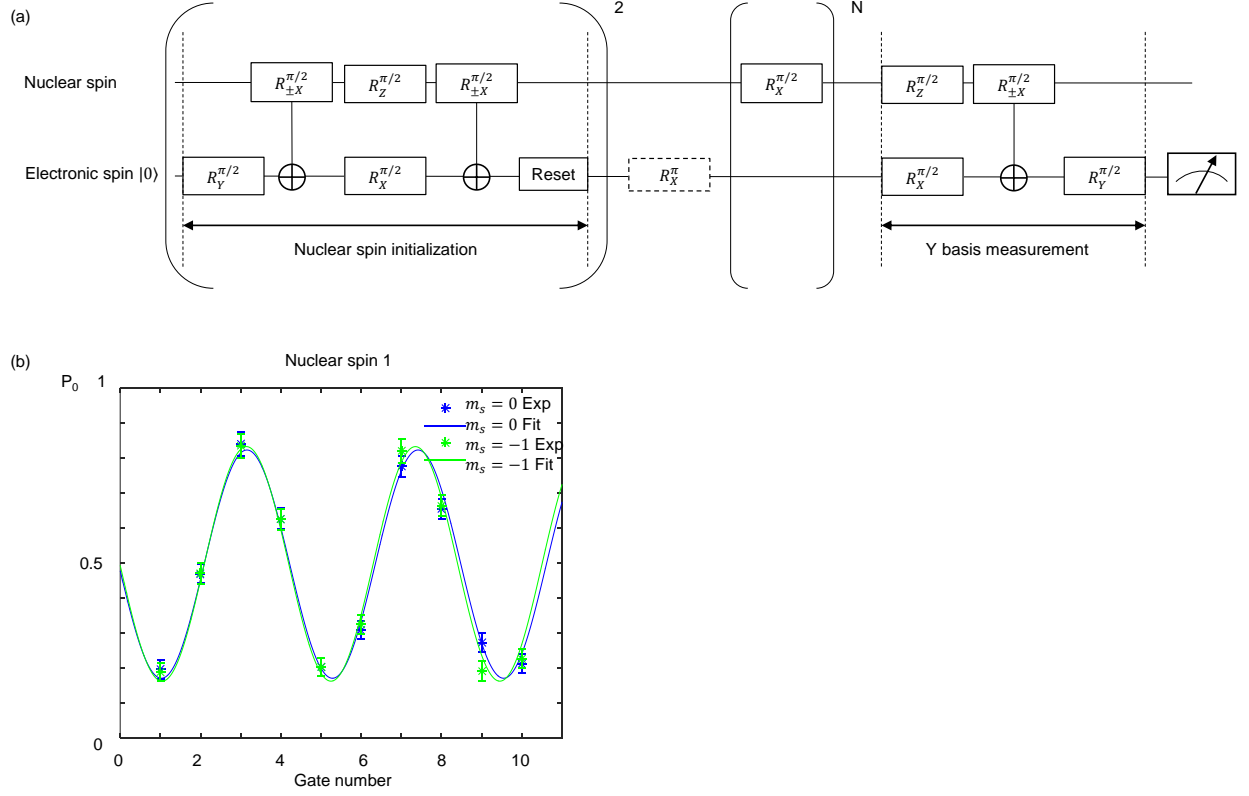


FIG. 4: Characterization of the unconditional X gate for nuclear spin 1. (a) Experimental scheme. The nuclear spin is polarized by swapping the electronic spin polarization onto the nuclear spin. An optional π rotation is applied to set the electronic spin to $m_s = -1$ state. After that, the desired gate is applied on the nuclear spin for $N = 1, \dots, 10$ times with electronic spin at $m_s = 0$ or $m_s = -1$ separately before measuring the nuclear spin on the Y basis. (b) Characterization of unconditional X gate for nuclear spin 1. Solid lines are fits by the formula $\sin(2\pi N/4) * (1 - bN)$ with $b = 0$ and a standard deviation $\sigma = 0.013$.

Assume the unpolarized nuclear spin is in a completely mixed state ρ_m , the state of the initialized electronic spin and a single nuclear spin is:

$$\rho = \rho_e \otimes \rho_n = p_1(\rho_0 \otimes \rho_m) + p_2(\rho_m \otimes \rho_m) + p_3(\rho_s \otimes \rho_m) + p_4(\rho_c \otimes \rho_m) \quad (11)$$

After swapping the nuclear spin with the electronic spin

$$\rho = p_1(\rho_m \otimes \rho_0) + p_2(\rho_m \otimes \rho_m) + p_3(\rho_s \otimes \rho_m) + p_4(\rho_c \otimes \rho_m) \quad (12)$$

Under the scenario that re-initialization of the electronic spin has no memory for the charge state, the state becomes:

$$\rho = (p_1\rho_0 + p_2\rho_m + p_3\rho_s + p_4\rho_c) \otimes (p_1\rho_0 + (1 - p_1)\rho_m) \quad (13)$$

Reading out the nuclear spin involves another swap gate between the nuclear and the electronic spin:

$$\rho = p_1(p_1\rho_0 + (1 - p_1)\rho_m) \otimes \rho_0 + p_2(p_1\rho_0 + (1 - p_1)\rho_m) \otimes \rho_m + p_3\rho_s \otimes (p_1\rho_0 + (1 - p_1)\rho_m) + p_4\rho_c \otimes (p_1\rho_0 + (1 - p_1)\rho_m) \quad (14)$$

Reading out electronic spin using green laser only yields non-zero signal for the electronic spin in the pure state ρ_0 . Thus the maximum signal contrast is:

$$C_{max} = \frac{p_1^2 + p_1 p_2}{p_1} = p_1 + p_2 \quad (15)$$

so that the maximum initialization and readout fidelity is calculated by:

$$F_{max} = \frac{1}{2} + \frac{C_{max}}{2} = \frac{1}{2} + \frac{p_1 + p_2}{2} \quad (16)$$

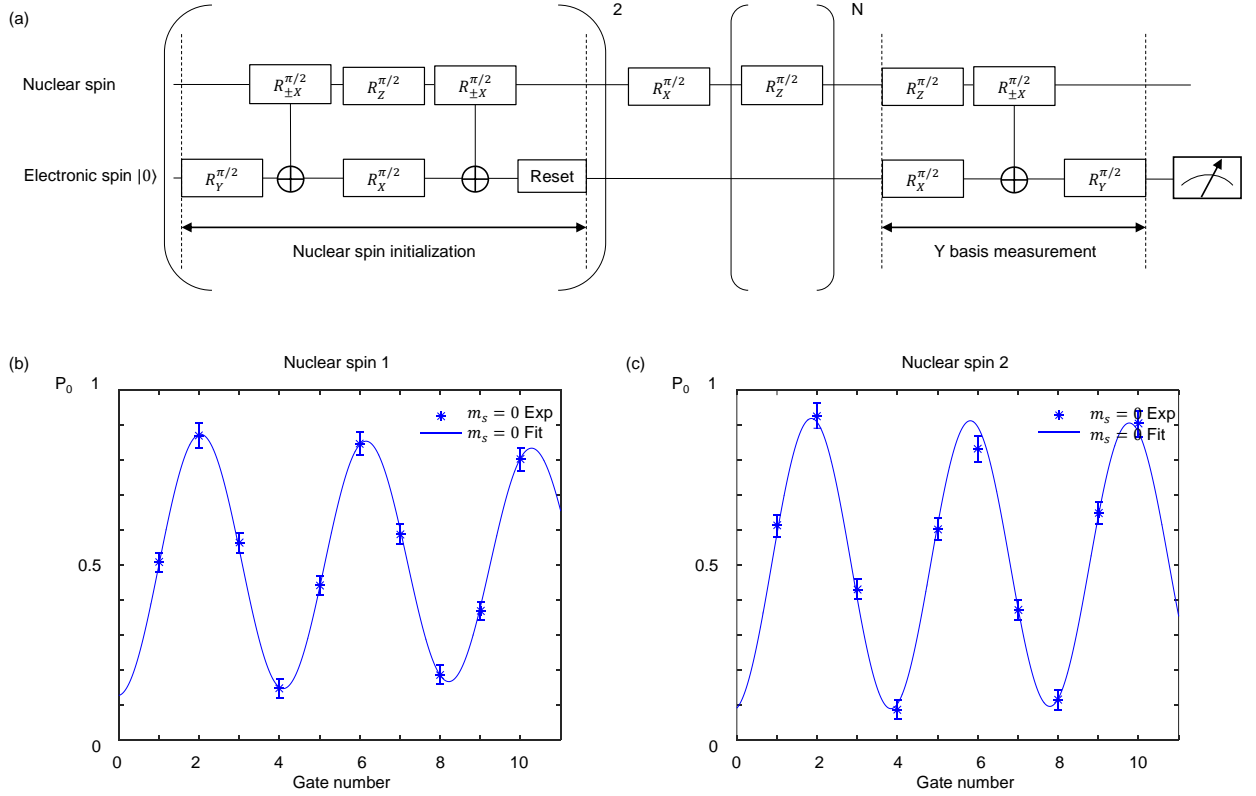


FIG. 5: Characterization of the unconditional Z gate for nuclear spin 1 and spin 2. (a) Experimental scheme. The nuclear spin is polarized by swapping the electronic spin polarization onto the nuclear spin. A $\pi/2$ rotation is applied to set the nuclear spin to $(|0\rangle - i|1\rangle)/\sqrt{2}$ state. After that, the desired gate is applied on the nuclear spin for $N = 1, \dots, 10$ times with electronic spin at $m_s = 0$ state before measuring on the Y basis. (b,c) Characterization of unconditional Z gate for nuclear spin 1 and spin 2. Solid lines are fits by the formula $\sin(2\pi N/4) * (1 - bN)$ with $b = 0.013$ and a standard deviation $\sigma = 0.006$ in (b), and with $b = 0.004$ and a standard deviation $\sigma = 0.015$ in (c)

From the above equation and the initialization and readout fidelity measured in the experiment (~ 0.9), we find $p_1 + p_2 \sim 0.8$, thus the charge state initialization fidelity $p_1 + p_2 + p_3 > 0.8$ under this scenario.

Alternatively, if the electron re-initialization does not change the charge state, the state after re-initialization becomes:

$$\rho = p_1 \left(\frac{p_1 \rho_0 + p_2 \rho_m + p_3 \rho_s}{p_1 + p_2 + p_3} \otimes \rho_0 \right) + (p_2 + p_3) \left(\frac{p_1 \rho_0 + p_2 \rho_m + p_3 \rho_s}{p_1 + p_2 + p_3} \otimes \rho_m \right) + p_4 \rho_c \otimes \rho_m \quad (17)$$

After another swap gate,

$$\rho = p_1 \left(\rho_0 \otimes \frac{p_1 \rho_0 + p_2 \rho_m}{p_1 + p_2 + p_3} \right) + p_1 \left(\frac{p_3 \rho_s}{p_1 + p_2 + p_3} \otimes \rho_0 \right) + (p_2 + p_3) \left(\rho_m \otimes \frac{p_1 \rho_0 + p_2 \rho_m}{p_1 + p_2 + p_3} \right) + (p_2 + p_3) \left(\frac{p_3 \rho_s}{p_1 + p_2 + p_3} \otimes \rho_m \right) + p_4 \rho_c \otimes \rho_m \quad (18)$$

So that the maximum initialization and readout fidelity becomes:

$$F_{max} = \frac{1}{2} + \frac{p_1 + p_2}{2(p_1 + p_2 + p_3)} \quad (19)$$

This indicates that the initialization and readout fidelity is independent of the charge state initialization fidelity.

TWO-BIT QUANTUM STATE TOMOGRAPHY

The two-bit tomography consists of three-basis (X, Y, Z) single-bit measurements on the two nuclear spins separately and nine two-bit correlation measurements. All the measurements are performed by mapping the nuclear spin

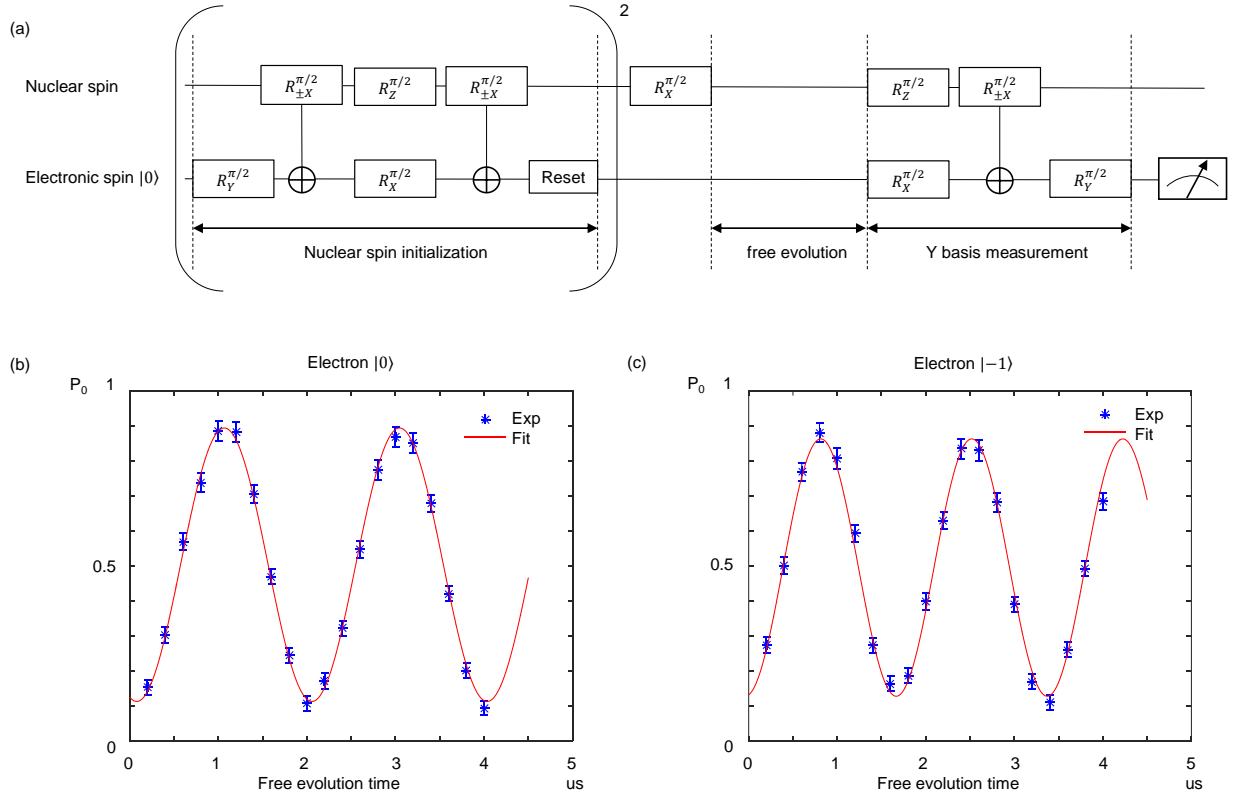


FIG. 6: Characterization of the initialization and readout fidelity for nuclear spin 1 and spin 2. (a) Experimental scheme. The nuclear spin is prepared to $(|0\rangle - i|1\rangle)/\sqrt{2}$ state by a $\pi/2$ rotation after the polarization. The measurement is performed by swapping the nuclear coherence onto the electronic spin polarization. The initialization and readout fidelity is obtained by measuring the contrast of the evolution. (b,c) Free evolution for nuclear spin 1 and spin 2 as a function of evolution time.

information onto the electronic spin population. Figure 7 shows our experimental scheme for the single-bit and two-bit measurements. The nuclear spin density matrix is extracted from the two-bit tomography result with a maximum likelihood calculation [3].

NUMERICAL SIMULATION

The numerical simulation is performed in the rotating frame in the three-qubit system composed of electronic spin and the two target nuclear spins. We assume a noiseless environment without decoherence and relaxation. The 350 ns green laser pumping is simulated by an instant reset of the electronic spin. After the reset, the nuclear spin state is given by the partial trace over the electronic spin state. All the parameters in the simulation is the same as those calibrated by the experiments.

CROSSTALK BETWEEN THE TWO NUCLEAR SPINS

As the nuclear hyperfine interactions are always on, gates on one nuclear spin will affect other nuclear spins and lead to unwanted operations. There are two types of possible operations on other nuclear spins: (i) Conditional or unconditional X operations. (ii) Z rotations.

Because conditional and unconditional X operations only happen at specific time τ with a very narrow bandwidth, the first type of influence can be avoided by choosing τ to bypass X rotations on other nuclear spins. To reduce the influence from the unwanted Z rotation, we track the phase of each nuclear spin in experiment through simulation and compensate accumulated phase at proper time in experimental sequence using the right parameters fixed from

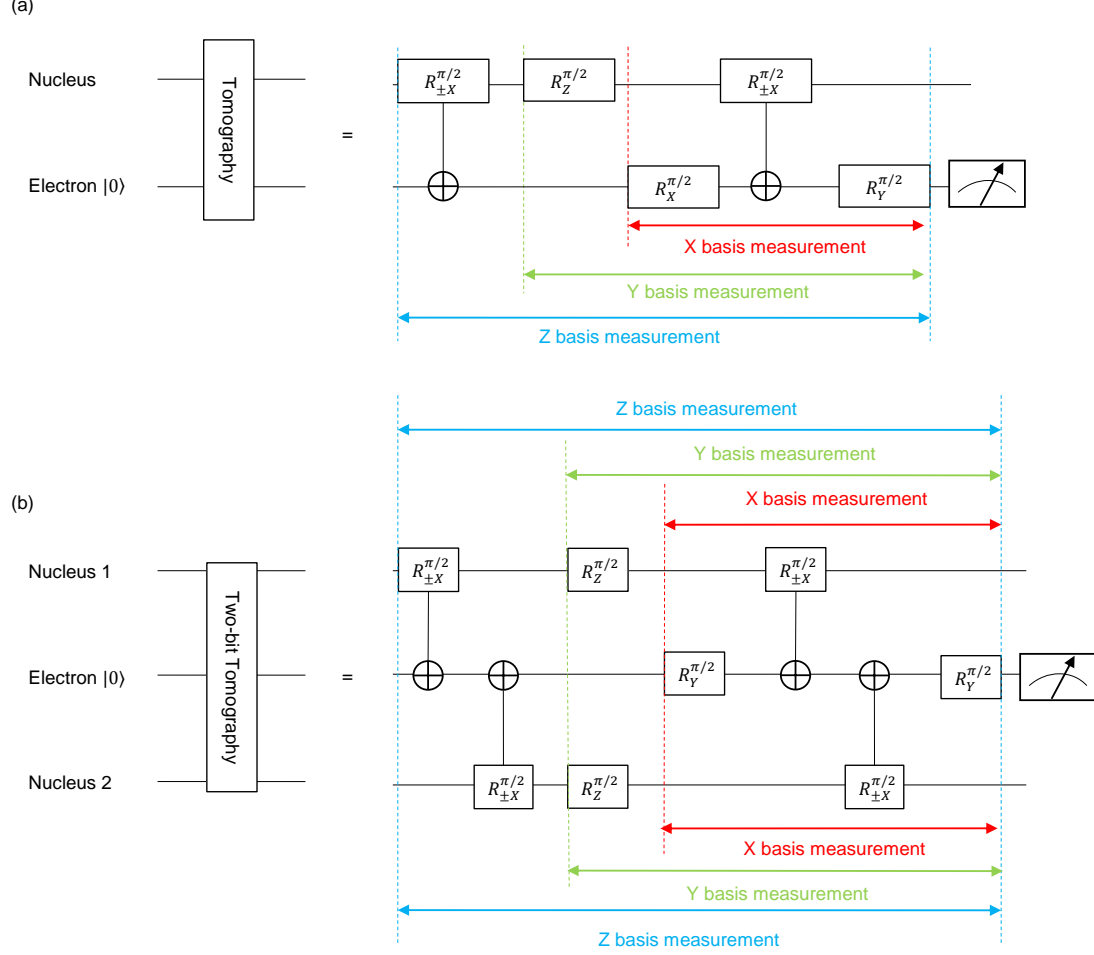


FIG. 7: Quantum state tomography scheme. (a) Single-bit tomography scheme of the three bases on the two nuclear spins separately. (b) Correlation measurements of the 9 bases on the two nuclear spins cooperatively.

the simulation.

REALIZATION OF GENERAL COLLECTIVE NOISE MODEL

By injecting radio frequency (rf) noise into the system to drive the nuclear spin transitions, we can realize any collective noise model. The rf signal is centered at the nuclear spin Larmor frequency with a bandwidth of 10 kHz. To model a noisy environment with time correlation function of the shape $\exp(-R|\tau|)$, we add up all the frequency components weighted with function $\sqrt{\frac{2\delta\omega R}{(2\pi n\Delta\omega)^2 + R^2}}$, where $\Delta\omega = 1$ kHz is the discretization step. The noise is turned on $5 \mu\text{s}$ after the entanglement preparation step and turned off $5 \mu\text{s}$ before the state tomography measurement to avoid the ac Stark shift on the electronic spin caused by the rf signal.

INFLUENCE OF THE MAGNETIC FIELD FLUCTUATION

The magnetic field is calibrated by measuring electronic ODMR signal every two hours during the experiments. Due to the fluctuation in the lab temperature, the magnetic field fluctuates on the order of 0.2 G. The fluctuation leads to gate errors accumulated on nuclear spin 1 as well as unwanted phase evolution on nuclear spin 2 in the entangling process. The induced phase fluctuation over the 10^6 repetitions of measurements of each experimental density matrix

element leads to a drop of the measured entanglement fidelity. In our numerical simulation, we find that a magnetic field fluctuation with a Gaussian shape and a standard deviation of 0.15 G leads to dropping of the entanglement fidelity from 1 to 0.92.

-
- [1] C. Zu, W.-B. Wang, L. He, W.-G. Zhang, C.-Y. Dai, F. Wang, L.-M. Duan, *Nature* 514, 72 (2014).
 - [2] T. H. Taminiau, J. J. T. Wagenaar, T. van der Sar, F. Jelezko, V. V. Dobrovitski and R. Hanson, *Phys. Rev. Lett.* 109, 137602 (2012).
 - [3] Daniel F. V. James, Paul G. Kwiat, William J. Munro, and Andrew G. White, *Phys. Rev. A* 64, 052312 (2001).
 - [4] P. C. Maurer, G. Kucsko, C. Latta, L. Jiang, N. Y. Yao, S. D. Bennett, F. Pastawski, D. Hunger, N. Chisholm, M. Markham, D. J. Twitchen, J. I. Cirac, M. D. Lukin, *Science* 336, 1283 (2012).
 - [5] J. Cramer, N. Kalb, M. A. Rol, B. Hensen, M. S. Blok, M. Markham, D. J. Twitchen, R. Hanson, T. H. Taminiau, *Nat. Commun.* 7: 11526 (2016).
 - [6] T. H. Taminiau, J. Cramer, T. van der Sar, V. V. Dobrovitski and R. Hanson, *Nature Nanotech.* 9, 171-176 (2014).